Thermomigration tuning of YBa(Formula presented) (Formula presented)Cu(Formula presented) (Formula presented)O(Formula

Citation for the original published paper (version of record):
Garibaldi, A., Trabaldo, E., Lombardi, F. et al (2026). Thermomigration tuning of YBa(Formula presented) (Formula presented)Cu(Formula presented) (Formula presented)O(Formula presented) (Formula presented)grooved Dayem nanoBridge-based SQUIDs. Superconductor Science and Technology, 39(7).
http://dx.doi.org/10.1088/1361-6668/ae7877

Superconductor Science and Technology

PAPER • OPEN ACCESS

Thermomigration tuning of $YBa_2Cu_3O_{7-\delta}$ grooved Dayem nanoBridge-based SQUIDs

To cite this article: Alessia Garibaldi *et al* 2026 *Supercond. Sci. Technol.* **39** 075008

Superconductor Science and Technology

Check for updates

OPEN ACCESS

RECEIVED
18 November 2025

REVISED
24 April 2026

ACCEPTED FOR PUBLICATION
4 June 2026

PUBLISHED
2 July 2026

PAPER

Thermomigration tuning of $YBa_2Cu_3O_{7-\delta}$ grooved Dayem nanoBridge-based SQUIDs

Alessia Garibaldi[1,2,*], **Edoardo Trabaldo**[1], **Floriana Lombardi**[1], **Justin F Schneiderman**[2] and **Thilo Bauch**[1]

[1] Quantum Device Physics Laboratory, Department of Microtechnology and Nanoscience, Chalmers University of Technology, SE-41296 Gothenburg, Sweden

[2] Department of Clinical Neuroscience, Institute of Neuroscience and Physiology, Sahlgrenska Academy, University of Gothenburg, SE-405 30 Gothenburg, Sweden

[*] Author to whom any correspondence should be addressed.

E-mail: alessiag@chalmers.se and bauch@chalmers.se

Keywords: YBCO, thermomigration, SQUID, GDB, optimization, *ex-situ*

Abstract

Thermomigration (TM) is an *ex-situ* technique that enables tuning of the transport properties in $YBa_2Cu_3O_{7-\delta}$-based nanostructures by driving oxygen migration through local Joule heating. We apply an AC current bias to conduct TM on grooved Dayem nanoBridge (GDB)-based Superconducting Quantum Interference Devices (SQUIDs) and investigate its impact on transport characteristics via current–voltage and voltage modulation measurements. By adjusting both the timing and amplitude of the applied AC bias, we identified two distinct TM modes: a 'hard' regime, characterized by high-bias, rapidly repeated AC-current bursts that reduce the critical current, and a 'soft' regime, in which lower-bias bursts separated by longer waiting times selectively tune the differential resistance at the operating point. Both tuning methods significantly enhance device performance, with voltage modulation improvements higher than a factor 5. Our findings confirm TM as a powerful post-fabrication tool for optimization of the transport properties of GDB-based high temperature superconductor SQUIDs.

1. Introduction

Superconducting Quantum Interference Devices (SQUIDs) are utilized in a wide range of fields, such as geophysical surveys [1], scanning microscopy [2], nanomagnetism [3], and biomagnetism [4]. The discovery of cuprate-based high temperature superconductors (HTSs) was an important step in SQUID development, making their applications no longer limited by the low availability and high cost of liquid Helium, since they could now be operated at liquid nitrogen temperature, i.e. $T = 77$ K, [5–10].

State-of-the-art HTS SQUIDs are achieved with grain boundary (GB)-based structures, such as bicrystal and step-edge junctions [8, 9, 11, 12]. However, fabrication of step-edge junctions is challenging [13], requiring multiple lithography steps, while the chip-to-chip reproducibility of bicrystal-based GB junctions is limited by that of the underlying bicrystal substrates.

The recent advancement of grooved Dayem bridge (GDB) weak links in $YBa_2Cu_3O_{7-\delta}$ (YBCO) has enabled the fabrication of SQUID magnetometers with magnetic field noise at 77 K on par with the best single-layer devices [14]. Unlike bicrystal junctions, GDBs can be positioned freely on the chip, oriented in any direction within the film plane, and do not rely on bicrystal substrates. Additionally, both the bridge and its groove are created in a single lithography step. However, GDBs also face reproducibility issues, which can pose a major limitation in applications that require SQUID arrays operating under the same ambient conditions, e.g. in multi-channel magnetoencephalography systems [15].

An important parameter of a SQUID is its magnetic flux noise, which reaches optimal performance when the screening parameter, $\beta_L = I_C L_{SQ}/\Phi_0$, is approximately equal to 1, where I_C is the SQUID's critical current, L_{SQ} its inductance, and Φ_0 the superconducting flux quantum. For β_L values above 1, the SQUID's voltage modulation depth $\Delta V \propto 1/(\beta_L + 1)$ becomes smaller. As a consequence, the total flux noise increases, since the contribution arising from the preamplifier's voltage noise grows according to $S_{\Phi,el}^{1/2} = S_{V,el}^{1/2}/\pi\Delta V$. Therefore, the resulting flux noise scales as $S_{\Phi,el} \propto 1/(\Delta V)^2$ [16, 17]. Chip-to-chip variations in I_C and resistance can then lead to a higher flux noise: too high I_C pushes β_L out of the optimal condition, while too small differential resistance at the operational point limits the maximum voltage modulation depth that can be expected. The maximum ΔV in a GDB is strongly linked to the product $\Delta I_C \delta R$ [18], where ΔI_C is the critical-current modulation depth and δR is the differential resistance evaluated at the operating point, that is, at the bias current for which the voltage modulations reach their maximum.

A promising approach to address this challenge with HTS SQUIDs involves *ex-situ* techniques such as electromigration (EM) [19, 20] and thermomigration (TM) [21], both of which enable tuning of the transport properties of a weak link post-fabrication. EM, a technique extensively studied in both low-temperature superconductor [22, 23] and HTS structures [24–27], drives atom migration through the application of high-bias DC currents or unipolar pulse trains, combining electric field forces and heating. In contrast, TM moves oxygen solely through a thermal gradient. In the TM method, a fast bipolar AC current is applied along the SQUID's weak links with an amplitude significantly exceeding the critical current and a frequency ($f \simeq 1$ kHz) much faster than the typical oxygen diffusion timescale across the groove, estimated at about 4 s [19]. Under these conditions, field-driven oxygen migration is negligible. Instead, oxygen moves primarily due to the thermal gradient between the constriction and the adjacent electrodes [28].

This localized heating mechanism differs in focus and behavior from thermal annealing [29], where a large portion on the device or the whole chip is heated and oxygen diffuses out of the material, leading to aging.

In YBCO, both EM and TM have been employed to reduce the doping of bare Dayem bridges, but only TM has demonstrated the ability to achieve this reduction uniformly across the bridge [26]. Moreover, we have previously demonstrated a drastic improvement in the voltage modulation depth of bare Dayem bridge weak links in YBCO SQUIDS with this *ex-situ* approach [21].

In this work, we present the effect of applying TM to GDB-based SQUIDs and identify two different TM approaches for tuning their weak-link transport properties. The first, called 'hard' TM, is a non-adiabatic TM approach that uses rapidly increasing AC bias pulse amplitudes and short intervals between pulses, preventing the system from reaching equilibrium between pulses. This regime enables significant reduction in I_C, bringing β_L closer to 1, increasing the voltage modulation depth, and therefore proving effective for SQUIDs with very large I_C. The second regime, referred to as 'soft' TM, is more adiabatic: it uses lower pulse amplitudes on average and longer inter-pulse intervals, allowing the system to re-equilibrate between pulses. We find that 'soft' TM more effectively shifts the SQUID operating point toward higher differential resistance, thereby enhancing voltage modulation through an increase of $\Delta I_C \delta R$, while leaving I_C largely unchanged.

2. GDB SQUIDs fabrication and TM

The SQUID fabrication process is started with the deposition of a 70 nm-thick, c-axis oriented YBCO film onto a (001)-oriented $SrTiO_3$ substrate by pulsed laser deposition (PLD). The deposition parameters are tuned to obtain a near optimally doped film with a critical temperature of approximately $T_c \simeq 89$ K. A 100 nm thick amorphous carbon layer is then deposited by PLD on top of the YBCO and patterned using electron beam lithography, followed by oxygen plasma reactive ion etching. The carbon mask pattern is subsequently transferred into the YBCO film via low-energy (300 eV) argon ion milling [30]. GDBs are defined by introducing a narrow gap across the full width of a short Dayem bridge in the carbon mask [14], with typical gap lengths l on the order of several tens of nanometers. Importantly, when the mask thickness to gap length ratio exceeds 2 ($t_C/l > 2$), the etch rate inside the nanogap decreases due to enhanced redeposition effects [31], resulting in a reduced effective ion milling rate. This process results in a nanobridge with a central groove, which serves as the weak link of the SQUID, as sketched in figure 1(b).

A scanning electron microscope image of a standard GDB-based SQUID, like the ones used for this work, is shown in figure 1(a), along with the current biasing and voltage probing schematics. The weak links are situated at the bottom of the hairpin SQUID loop, connecting the loop to the bottom SQUID electrode. The loop has a length of 8 μm, a slit width of 0.5 μm and line width of 2 μm, while the GDBs have a length of $L \simeq 150$ nm, and a width in the range $w = 200 - 300$ nm. The SQUID is connected to a primary current source, I_b, which is used to bias the SQUID junctions and the voltage across the SQUID is amplified by a low-noise amplifier. At low bias levels, this setup allows for measurement

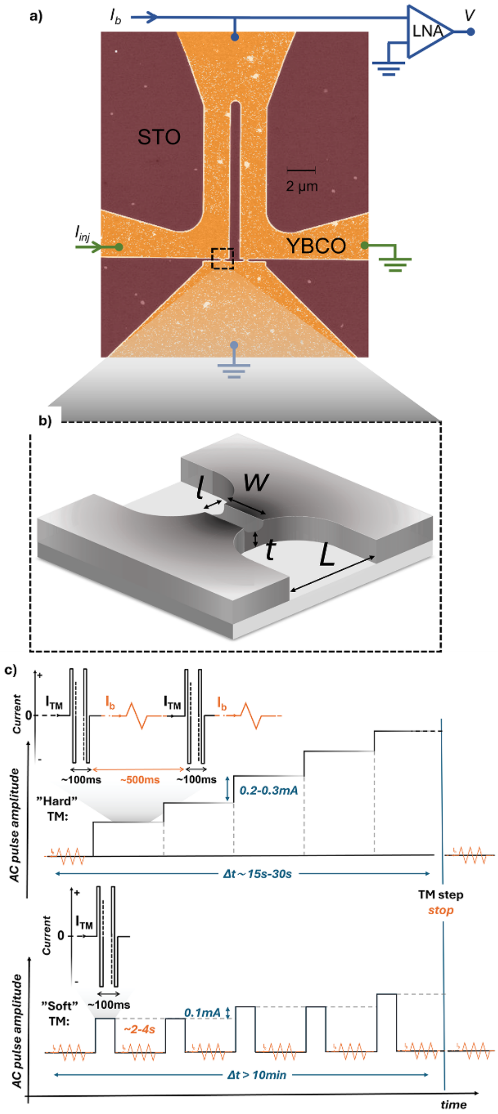

Figure 1. (a) Scanning electron microscope image in false colors of a GDB-based SQUID. The image includes a schematic of the measurement system, where I_{inj} is the current injection, and I_b is the bias current. (b) Sketch of a GDB with gap width w, length l, thickness t and bridge length L. (c) Schematic illustration of the timing and amplitude profiles of the square-wave AC-current pulses in the 'hard' (upper panel) and 'soft' (lower panel) regimes and between; see main text for details.

of the device's current voltage characteristics (IVCs), while at higher bias levels, it enables TM of the GDBs. Additionally, a secondary current source is connected to the SQUID loop to inject a current I_{inj}, which modulates the phase difference between the two weak links $\Delta\varphi = 2\pi L_{loop} I_{inj}/\Phi_0$, where L_{loop} is the inductance of the hairpin loop.

All measurements and TM steps in this work were conducted with the SQUIDs mounted in a dipstick immersed in liquid nitrogen with ∼200 mbar of He thermal exchange gas such that the sample temperature was ∼82 K. After fabrication, we first measured the IVC of the SQUID using bias currents I_b ranging from 3 to 5 times the critical current I_C. We then swept the injection current I_{inj} and monitored the resulting voltage modulation amplitude while ramping I_b to identify the bias current point (the operational point) that yielded the maximum peak-to-peak voltage modulation, i.e. the modulation depth ΔV. The initial characterization of the SQUIDs is indicated as IV0 in figures 2 and 3. To assess the effect of TM on SQUID performance, we compared the IVC and voltage modulation depth ΔV before and after each TM treatment, e.g. TM1 as compared to IV0.

The TM procedure consisted of repeatedly applying 1 kHz square-wave bipolar current bursts, centered at zero. Each burst lasted 100 ms.

After each burst, the IVC of the SQUID was measured using bias currents that are significantly lower than those applied during the TM process. This approach allowed for monitoring of the evolution of the SQUID's transport properties such as the critical current I_c and the differential resistance δR after the application of each TM burst.

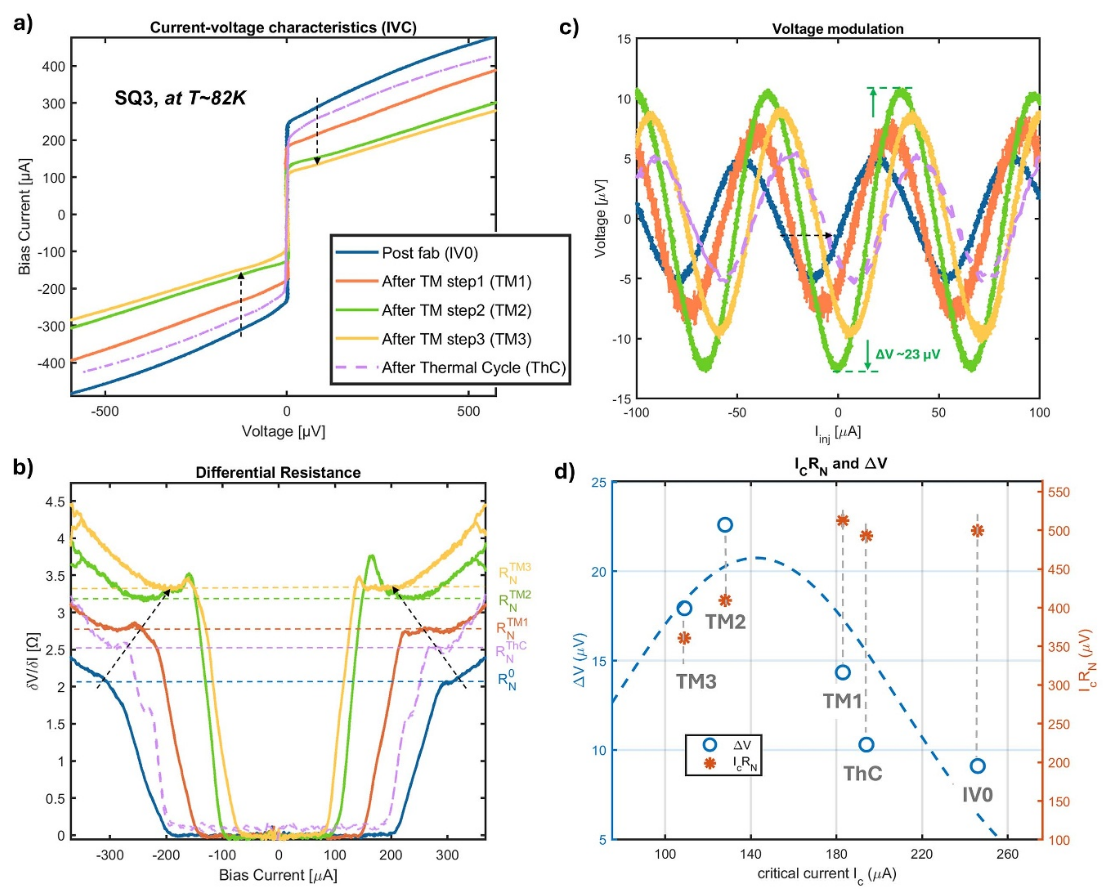

Figure 2. Critical-current reduction thermomigration ('hard' TM) effects on (a) current–voltage characteristics (IVC), (b) differential resistance ($\delta V/\delta I$), (c) voltage modulation, and (d) $I_C R_N$ and ΔV of SQUID3 (SQ3), the device that yielded the highest post-TM ΔV. Characterization right after fabrication is labeled as IV0, while TM1, TM2 and TM3 indicate the state of the SQUID after each step of TM. Arrows in (a), (b) and (c) indicate the sample's evolution across the TM steps, from post fab through application of the third TM-pulse, which finally resulted in a reduction in both $I_C R_N$ and ΔV. The thermal cycle (ThC) data was collected last, after all thermomigration steps were concluded. A flux-offset was also manually introduced in (c) to improve the figure's readability. In (d), the dashed line is a guide to the eye for ΔV as a function of I_C. Note the partial 'recovery' of the sample's post-fabrication properties after thermal cycling, indicating potential temperature-induced back-migration of oxygen into the GDBs.

The TM approach for each device was selected based on its transport properties: those with excessive I_C received 'hard' TM; those with acceptable I_C but low δR at the operational point underwent 'soft' TM. A simplified depiction of the two approaches is shown in figure 1(c).

In the 'hard' TM approach, the AC current bursts were rapidly ramped to high amplitudes, sometimes reaching current densities well above the typical oxygen migration threshold of 15–17 MA cm^{-2} [26]. The bursts were applied continuously, separated only by brief ∼500 ms pauses. This process was continued until a significant change in I_C was observed in the IVC measurements. Because the intervals between bursts are so short, the system cannot relax to equilibrium, making this a distinctly non-adiabatic process. Indeed, even after the final burst, we observe that the IVC continues to evolve over the following second, demonstrating that the relaxation timescale is significantly longer than the burst spacing and that the cumulative heating drives a rapid reduction of the superconducting properties.

In the 'soft' TM approach, on average lower-amplitude AC single bursts (i.e. just above the threshold for oxygen migration) were delivered with extended pauses of several seconds in between them (∼2–4 s), where only I_b was swept (triangular waveforms in figure 1) for continuous monitoring of the IVC. These extended pauses allowed for thermalization in between bursts and relaxation of the system into an equilibrium state. This state could then be correctly measured in the IVC before the next TM burst was applied. This made this second process more adiabatic in nature.

Pulses were no longer applied once a measurable change in the differential resistance was observed; the voltage modulation characteristics were then recorded again.

After a maximum of three steps of TM all the devices were thermally cycled (ThC) by warming the devices to room temperature (300 K) and a few hours later cooled again. Devices were then re-characterized; in addition, a magnetic flux noise measurement was performed on one device.

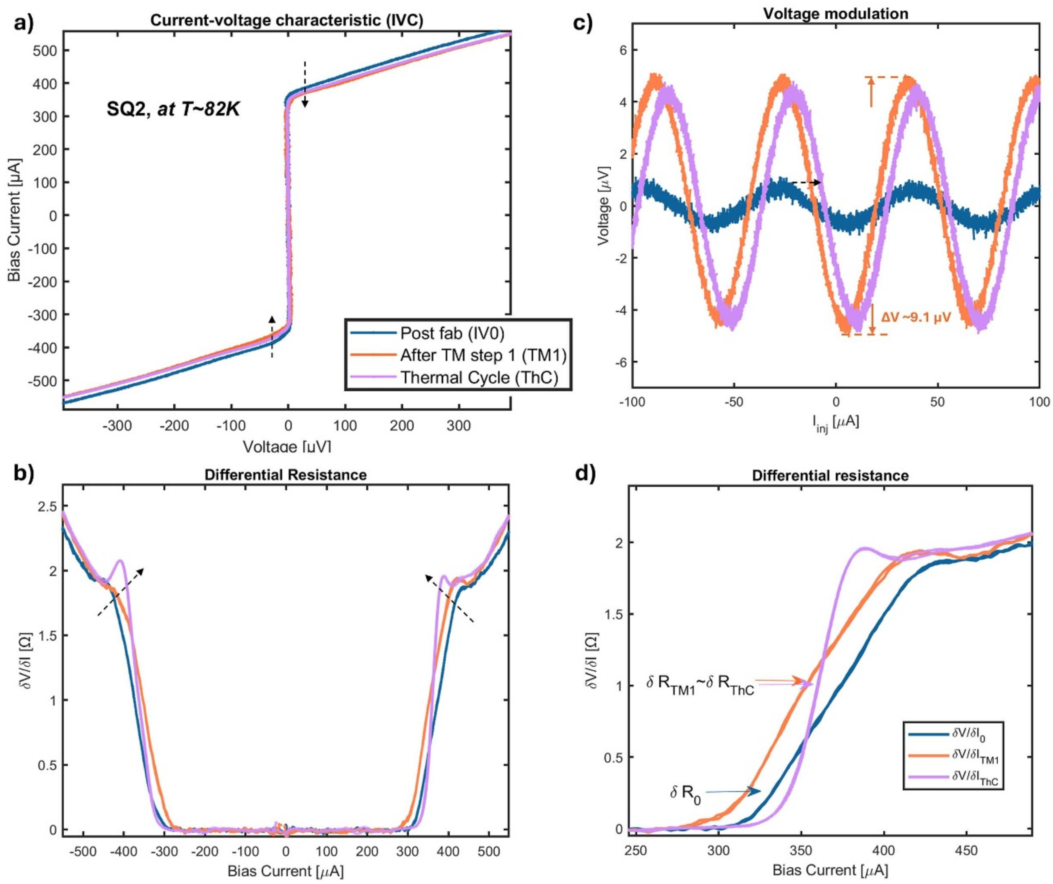

Figure 3. Differential resistance tuning thermomigration ('soft' TM) effects on (a) current–voltage characteristics (IVC), (b) differential resistance ($\delta V/\delta I$), (c) voltage modulation (ΔV) and (d) zoomed-in of differential resistance of SQUID2 (SQ2). Characterization right after fabrication is labeled as IV0, while TM1 indicates the state of the SQUID after one step of TM. Arrows in (a), (b) and (c) indicate the sample's evolution from post fabrication and after one application of TM. Finally, measurements after thermal cycle (ThC) were conducted. A flux-offset was also manually introduced in (c) to improve the figure's readability. In (d) we show the treatment effect on the operational point for differential resistance, δR of the device. We see that after just one TM application the differential resistance at the operational point has increased substantially, motivating the enhancement in voltage modulations, while I_C results relatively unchanged. After ThC, almost no effect due to thermally-induced oxygen back-migration was recorded.

3. Results and discussion

Several GDB-based SQUID devices with groove length $l = 30 - 50$ nm and width $w = 200 - 300$ nm were subjected to TM in this work. The results of successive TM procedures are summarized in table 1, where we show the evolution of the critical current I_C and maximum voltage modulation depth ΔV after each TM step.

3.1. 'Hard' TM

The results for the subset of devices where TM was used to lower the critical current, thereby reducing the screening parameter β_L to enhance ΔV, are presented in table 1 for SQ1,3,6,7 and 8.

To achieve this, we applied AC current bursts with amplitudes well above the threshold for TM ($\simeq$2 mA) reaching values up to 7.8 mA. The best result from applying this type of TM protocol was obtained for device SQ3, as shown in figure 2. Panel (a) displays the evolution of the current–voltage characteristics right after fabrication and before treatment (Post Fab) and after three consecutive TM treatments (TM1-3). The IVC is also recorded following a thermal cycle (ThC) of the SQUID through room temperature (Post ThC). The corresponding differential resistances and voltage modulations at the optimal working points are shown in panels (b) and (c), respectively. In the following, we examine how the voltage modulation depth ΔV evolves after each TM step, using an expression originally derived for SQUIDs with identical resistively shunted Josephson junctions (RSJ model) [32, 33]:

$$\Delta V = \frac{4}{\pi} \frac{I_C R_N}{1 + \beta_L} \exp\left(-3.5\pi^2 \frac{k_B T L_{SQ}}{\Phi_0^2}\right). \tag{1}$$

Table 1. Evolution of Voltage modulation depth at the operational point, ΔV, and critical current, I_C, for 7 GDB-based SQUIDs, for successive steps of thermomigration and a thermal cycling. All weak links presented here show an increase in their voltage modulations across thermomigration steps up until a maximum, after which the superconducting properties seem to quickly degrade. The nominal TM bias current density amplitudes, defined as I_{TM}/wt_f, with I_{TM} the AC current amplitude, w the bridge width, and t_f the film thickness, span a wide range for the SQUIDs listed in table, from as low as 13.5 MA cm^{-2} for SQ7 up to 55 MA cm^{-2} for SQ3. TM in both approaches was applied using a pulsed bipolar square waveform with frequency 1 kHz. In the 'hard' TM approach, bursts followed ∼500 ms interval of 'zero' bias, during which the current voltage characteristic was measured. In the 'soft' one, these 'zero' bias periods were longer, typically 2–4 s (see figure 1(c) for details).

GDB	Post-Fab	TM-protocol	TM1	TM2	TM3	ThC
*Width**length* nm*nm	I_C, ΔV µA, µV		I_C, ΔV µA, µV	I_C, ΔV µA, µV	I_C, ΔV µA, µV	I_C, ΔV µA, µV
SQ1: 30*200	433, 1	'Hard'	354, 3.1	306, 5	/	/
SQ3: 40*200	246, 9	'Hard'	183, 15	128, 23	109, 18	200, 10
SQ6: 30*300	733, 0	'Hard'	601, 2	499, 2.3	275, 1.5	432, 2.3
SQ7: 40*300	327, 3	'Hard'	243, 5.7	168, 16	122, 6	170, 5
SQ8: 40*300	437, 6	'Hard'	295, 11.5	143, 5	/	/
SQ2: 40*200	368, 2	'Soft'	348, 9.1	–,–	–,–	358, 8.7
SQ5: 50*200	60, 5	'Soft'	60, 8	52, 13	–,–	52, 5

Here, R_N denotes the normal-state resistance of the SQUID, k_B is the Boltzmann constant, and L_{SQ} is the SQUID inductance. Given that L_{SQ} and T are not affected by TM applications, the exponential term can be assumed to remain constant and be disregarded in the following discussion. In our analysis, R_N is extracted from the linear region of the IVCs above the critical current (indicated by the horizontal lines in figure 2(b)). While our weak links cannot be described accurately by the RSJ model, we believe that equation (1) still provides a useful first-order approximation for interpreting the changes in ΔV after TM.

The decrease in critical current I_C following both TM1 and TM2 steps, as seen in the IVCs in figure 2(a), was accompanied by a 2.5-fold increase in the voltage modulation depth ΔV, reaching up to 23 μV (see figure 2(c)). Figure 2(d) illustrates the evolution of the voltage modulation depth ΔV and the $I_C R_N$ product as functions of the critical current after each TM step. Since the small decrease in the $I_C R_N$ product after TM1 and TM2 (see figure 2(d)) would, if anything, lead to a reduction in ΔV, it cannot account for the observed increase. Thus, according to equation (1), the enhancement in ΔV must instead result, at least partially, from a decrease in the screening parameter β_L.

Indeed, β_L decreases from approximately 3.8 to 2.0 after the TM1 and TM2 steps, which, according to equation (1), corresponds to an expected increase in ΔV of roughly 65%. Although this estimated increase does not fully account for the total enhancement observed after TM, it does explain, and at least partially justify, the substantial rise in ΔV.

However, following a further decrease in critical current after the third TM step (TM3), ΔV no longer increases. Instead, a decrease is observed, likely due to a further drop in the $I_C R_N$ product (see figure 2(d)), suggesting a reduction in the weak link's critical temperature, consistent with our previous findings on Dayem bridge-based SQUIDs [21]. Overall, the 'hard' TM approach was able to significantly improve the voltage modulation performances in almost all cases, with ΔV increasing by more than a factor 5 as compared to its initial value (see table 1, SQ7). Surprisingly, this method was effective even for devices, such as SQ3 and 8, that initially exhibited sizable voltage modulations, in contrast to the findings reported in [21] for Dayem bridge-like structures.

3.2. 'Soft' TM

A smaller subsection of devices was subjected to the 'soft' TM approach, aiming to enhance ΔV without significantly reducing I_C. This method was oriented mainly at shifting the operational point of the SQUID to a higher differential resistance, as shown in figure 3. In the 'soft' TM approach, the AC current never exceeded 2.4 mA. Combined with improved thermalization between bursts, this allowed for precise tuning of the differential resistance at bias currents slightly above the critical current, rather than directly reducing the weak link's critical current.

Figure 3 presents the results obtained on SQ2 using the 'soft' TM protocol. After a single TM step, the critical current I_C remained nearly unchanged, whereas the voltage modulation depth ΔV was increased by a factor of 4.5 compared to the measured device right after fabrication (Post Fab), rising from 2 to 9.1 μV. As demonstrated in [18], the maximum voltage modulation can be approximated by $\Delta V \simeq \Delta I_C \delta R$, where ΔI_C is the modulation depth of the critical current and δR is the differential resistance at the optimal working point. Since the critical current, and consequently ΔI_C, is only minimally

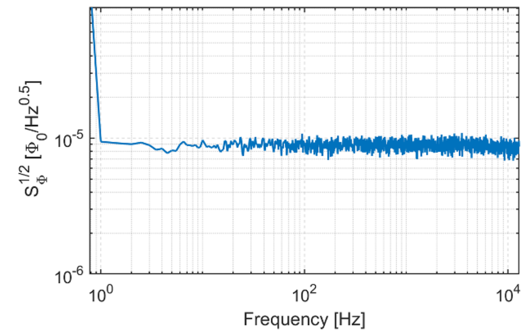

Figure 4. Magnetic flux noise characterization of the SQUID with the highest voltage modulation (SQ3) after TM and subsequent thermal cycling. This measurement was conducted in a different setup, at 77 K, with SQUID-specific electronics. From the plot it can be seen that the noise spectrum is flat, and thus white-noise dominated, down to 1 Hz.

affected by this type of TM procedure, the observed enhancement in ΔV is attributed to an increase in the differential resistance at the optimal working point (see arrows in figure 3(d)). One could argue that such a small change in I_C, combined with a substantial increase in ΔV, might result from magnetic flux trapping. However, the critical induction field required to trap magnetic flux in a GDB is given by $B_C = a^*(\Phi_0/w^2)$ [34], where w is the width of our weak-links (≃200–300 nm) and a a factor experimentally found to be around 1.55. This yields a minimum trapping field on the order of tens of mT. Given that our setup's background field is only about 50 μT, it is highly unlikely that any flux can be trapped in the bridges during the cool downs.

We speculate instead, that the observed increase in differential resistance results from a redistribution of oxygen within the constriction itself, rather than from oxygen migration into the broader electrodes. Nevertheless, the exact microscopic mechanism responsible for this effect remains unclear and is currently under investigation.

3.3. Thermal cycle and noise characterization

Once all TM steps had been performed and characterized, all the devices were thermally cycled (ThC) and then characterized again. Their final electrical performances are reported in table 1 and shown in figures 2 and 3 for both SQ3 and SQ2, respectively. During TM, particularly the 'hard' TM approach, oxygen is redistributed from its initial region near the groove toward the electrodes, thereby reducing the local doping in the bridge, while still remaining within the material. The oxygen in the CuO chains of YBCO is highly mobile, and thus it is unlikely for it to remain pinned at specific sites during this process. Since TM is conducted at low temperatures (∼82 K), the newly induced gradient in oxygen concentration will stay unchanged for as long as the system is kept cold, but when the device is subsequently warmed to room temperature, the increased oxygen mobility is expected to accelerate diffusion. This should promote partial or even complete back-diffusion of the thermomigrated oxygen, driven by the oxygen concentration gradient. Evidence of oxygen redistribution is seen in the ThC curves of SQ3 in figure 2. Along with the recovery of I_C, the enhanced voltage modulation ΔV was largely lost, though the device still outperformed its original state, with a post-thermal cycling value of 10 μV. Therefore, enhancements obtained through 'hard' TM application are not resistant to thermal cycling and the initial state of the SQUID is often at least partially reinstated, even after just one thermal cycle.

In contrast, 'soft' TM devices show greater resilience to thermal cycling, with less impact on performance. This is clearly seen in SQ2, where a single TM treatment followed by thermal cycling resulted in minimal changes to the IVC and a voltage modulation ΔV that remained high at 8.7 μV.

Finally, we performed a magnetic flux noise measurement $S_\phi^{1/2}$ on the device with the highest voltage modulation ΔV. This specific measurement was done at $T = 77$ K in a 2-layer magnetic shielded room using a commercial Magnicon SEL-1 dc-SQUID electronics [35] operated in flux-locked loop and AC-bias reversal (40 kHz) mode, the latter to reduce the 1/f noise contribution of critical current noise.

The magnetic flux noise is predominantly constant (white noise) down to frequencies of 1 Hz as shown in figure 4. The low white magnetic flux noise level $S_\phi^{1/2} \simeq 8\ \mu\Phi_0/\mathrm{Hz}^{0.5}$ is comparable to state of the art GB based YBCO SQUIDs [8, 9, 12, 17, 36]. Given the amplifier's input voltage noise of 0.4 nV/Hz$^{0.5}$ and transfer function of $\pi\Delta V \simeq 30\ \mu V/\Phi_0$, we find that the detected magnetic flux noise is mainly governed by the electronic component $S_{\Phi,el} \propto 1/(\Delta V)^2$ [16, 17], meaning that the TM steps did not significantly raise the SQUID intrinsic noise by introduction of any additional flux noise source in the device, as one would have expected if significant disorder was introduced.

4. Conclusions

TM has proven to be a promising technique for *ex-situ* optimization of HTS nanostructures, particularly in geometries with strongly confined current paths such as GDBs. This work demonstrates that TM can significantly enhance the performance of GDB-based SQUIDs, yielding competitive noise levels and robust voltage modulations. Our results show that most devices benefit from one or two TM steps, beyond which further treatment causes a degradation of performance. TM applied for reshaping the IVC, without reducing I_C, also showed considerable improvements and appeared more stable under thermal cycling.

Although thermal cycling currently constrains the applicability of TM for some practical SQUID technologies, future studies could explore hybrid TM protocols that combine different bias strategies or incorporate thermal cycling as an intermediate step. Other application areas can benefit from our TM process in its present form: in biomagnetic measurements, for example, SQUID magnetometers must be tuned and read out under optimal conditions during each cool down. Our method allows key SQUID parameters to be adjusted directly within the same measurement setup and the same cool down. This is especially valuable in multi-channel systems, such as those used for neuromagnetic field mapping in magnetoencephalography, where sensor-to-sensor variations in optimal bias current can be large enough to prevent all channels from high-performance operation at a fixed system temperature.

Finally, developing standardized TM procedures and conducting systematic noise measurements before and after treatment will be an essential future step in further investigating the full potential of this technique.

Acknowledgments

This work was performed in part at Myfab Chalmers. We acknowledge financial support from the Swedish Research Council (VR) under the Projects 2022-04334 (F. L.), 2020-05184 (T. B.), 2021-04032 (J. F. S.), and the European Union's Horizon Europe research and innovation program under Grant Agreement No. 101130224 (JOSEPHINE).

Data availability statement

The data that support the findings of this study are available upon reasonable request from the authors.

ORCID iDs

Alessia Garibaldi 0009-0009-0090-4601
Floriana Lombardi 0000-0002-3478-3766
Justin F Schneiderman 0000-0002-4441-2360
Thilo Bauch 0000-0002-8918-4293

References

[1] Stolz R, Chwala A, Zakosarenko V, Schulz M, Fritzsch L and Meyer H-G 2006 Seg technical program expanded abstracts
[2] Vasyukov D, Anahory Y, Embon L, Halbertal D, Cuppens J, Neeman L, Finkler A, Segev Y, Myasoedov Y and Rappaport M L A 2013 *Nat. Nanotechnol.* **8** 639
[3] Granata C and Vettoliere A 2016 *Phys. Rep.* **614** 1
[4] Körber R *et al* 2016 *Supercond. Sci. Technol.* **29** 113001
[5] Leslie K, Binks R, Lam S, Sullivan P, Tilbrook D, Thorn R and Foley C 2008 *Lead. Edge* **27** 70
[6] Hato T, Tsukamoto A, Adachi S, Oshikubo Y, Watanabe H, Ishikawa H, Sugisaki M, Arai E and Tanabe K 2013 *Supercond. Sci. Technol.* **26** 115003
[7] Chwala A, Stolz R, Schmelz M, Zakosarenko V, Meyer M and Meyer H-G 2015 *IEICE Trans. Electron.* **98** 167
[8] Öisjöen F, Schneiderman J F, Figueras G, Chukharkin M, Kalabukhov A, Hedström A, Elam M and Winkler D 2012 *Appl. Phys. Lett.* **100** 132601
[9] Faley M, Dammers J, Maslennikov Y, Schneiderman J, Winkler D, Koshelets V, Shah N and Dunin-Borkowski R 2017 *Supercond. Sci. Technol.* **30** 083001
[10] Schneiderman J F, Ruffieux S, Pfeiffer C and Riaz B 2019 Magnetoencephalography: from signals to dynamic cortical networks p 1313
[11] Schwarz T, Wölbing R, Reiche C F, Müller B, Martínez-Pérez M-J, Mühl T, Büchner B, Kleiner R and Koelle D 2015 *Phys. Rev. Appl.* **3** 044011

[12] Mitchell E and Foley C 2010 *Supercond. Sci. Technol.* **23** 065007
[13] Millar A, Romans E, Carr C, Eulenburg A, Donaldson G and Pegrum C 2001 *IEEE Trans. Appl. Supercond.* **11** 1351–4
[14] Trabaldo E, Pfeiffer C, Andersson E, Arpaia R, Kalaboukhov A, Winkler D, Lombardi F and Bauch T 2019 *Nano Lett.* **19** 1902
[15] Pfeiffer C, Ruffieux S, Jönsson L, Chukharkin M L, Kalaboukhov A, Xie M, Winkler D and Schneiderman J F 2020 *IEEE Trans. Biomed. Eng.* **67** 1483
[16] Tesche C D and Clarke J 1977 *J. Low Temp. Phys.* **29** 301
[17] Ruffieux S, Kalaboukhov A, Xie M, Chukharkin M, Pfeiffer C, Sepehri S, Schneiderman J F and Winkler D 2019 *Supercond. Sci. Technol.* **33** 025007
[18] Trabaldo E, Ruffieux S, Andersson E, Arpaia R, Montemurro D, Schneiderman J, Kalaboukhov A, Winkler D, Lombardi F and Bauch T 2020 *Appl. Phys. Lett.* **116** 132601
[19] Moeckly B, Lathrop D and Buhrman R 1993 *Phys. Rev. B* **47** 400
[20] Keijers W, Baumans X D A, Panghotra R, Lombardo J, Zharinov V S, Kramer R B G, Silhanek A V and Van de Vondel J 2018 *Nanoscale* **10** 21475
[21] Trabaldo E, Garibaldi A, Lombardi F and Bauch T 2021 *Supercond. Sci. Technol.* **34** 104001
[22] Lombardo J, Collienne S, Petrillo A A D, Fourneau E, Nguyen N D and Silhanek A V 2019 *New J. Phys.* **21** 113015
[23] Baumans X D A *et al* 2017 *Small* **13** 1700384
[24] Baumans X D, Fernández-Rodríguez A, Mestres N, Collienne S, Van de Vondel J, Palau A and Silhanek A V 2019 *Appl. Phys. Lett.* **114** 012601
[25] Lyatti M, Poppe U, Gundareva I and Dunin-Borkowski R E 2019 *Superconductivity*
[26] Trabaldo E, Kalabukhov A, Arpaia R, Andersson E, Lombardi F and Bauch T 2022 *Phys. Rev. Appl.* **17** 024021
[27] Marinković S, Stoffels D, Collienne S, Fernández-Rodríguez A, Mestres N, Palau A and Silhanek A V 2024 *Phys. Rev. B* **110** 165157
[28] Oriani R 1969 *J. Phys. Chem. Solids* **30** 339
[29] Vettoliere A, Ruggiero B, Valentino M, Silvestrini P and Granata C 2019 *Sensors* **19** 3635
[30] Nawaz S, Arpaia R, Lombardi F and Bauch T 2013 *Phys. Rev. Lett.* **110** 167004
[31] Emery-Adleman T and Taylor B J 2019 Understanding complex systems p 244
[32] Enpuku K, Tokita G and Maruo T 1994 *J. Appl. Phys.* **76** 8180
[33] Enpuku K and Enpuku K 1993 *Jpn. J. Appl. Phys.* **32** 1407
[34] Kuit K H, Kirtley J R, van der Veur W, Molenaar C G, Roesthuis F J G, Troeman A G P, Clem J R, Hilgenkamp H, Rogalla H and Flokstra J 2008 *Phys. Rev. B* **77** 134504
[35] Magnicon SQUID electronics SEL-1 (available at: www.magnicon.com)
[36] Chukharkin M, Kalabukhov A, Schneiderman J F, Öisjöen F, Jönsson M, Xie M, Snigirev O V and Winkler D 2013 *IEEE Trans. Appl. Supercond.* **23** 1602704